Generation of whistler mode emissions in the inner magnetosphere: An event study

D. Schriver,[1] M. Ashour-Abdalla,[1,2] F. V. Coroniti,[2] J. N. LeBoeuf,[3] V. Decyk,[2] P. Travnicek,[1,4] O. Santolík,[5,6] D. Winningham,[7] J. S. Pickett,[8] M. L. Goldstein,[9] and A. N. Fazakerley[10]

Received 28 September 2009; revised 6 April 2010; accepted 28 April 2010; published 21 August 2010.

[1] On July 24, 2003, when the Cluster 4 satellite crossed the magnetic equator at about 4.5 R_E radial distance on the dusk side (~15 MLT), whistler wave emissions were observed below the local electron gyrofrequency (f_{ce}) in two bands, one band above one-half the gyrofrequency ($0.5f_{ce}$) and the other band below $0.5f_{ce}$. A careful analysis of the wave emissions for this event has shown that Cluster 4 passed through the wave source region. Simultaneous electron particle data from the PEACE instrument in the generation region indicated the presence of a mid-energy electron population (~100 s of eV) that had a highly anisotropic temperature distribution with the perpendicular temperature 10 times the parallel temperature. To understand this somewhat rare event in which the satellite passed directly through the wave generation region and in which a free energy source (i.e., temperature anisotropy) was readily identified, a linear theory and particle in cell simulation study has been carried out to elucidate the physics of the wave generation, wave-particle interactions, and energy redistribution. The theoretical results show that for this event the anisotropic electron distribution can linearly excite obliquely propagating whistler mode waves in the upper frequency band, i.e., above $0.5f_{ce}$. Simulation results show that in addition to the upper band emissions, nonlinear wave-wave coupling excites waves in the lower frequency band, i.e., below $0.5f_{ce}$. The instability saturates primarily by a decrease in the temperature anisotropy of the mid-energy electrons, but also by heating of the cold electron population. The resulting wave-particle interactions lead to the formation of a high-energy plateau on the parallel component of the warm electron velocity distribution. The theoretical results for the saturation time scale indicate that the observed anisotropic electron distribution must be refreshed in less than 0.1 s allowing the anisotropy to be detected by the electron particle instrument, which takes several seconds to produce a distribution.

Citation: Schriver, D., et al. (2010), Generation of whistler mode emissions in the inner magnetosphere: An event study, *J. Geophys. Res.*, *115*, A00F17, doi:10.1029/2009JA014932.

1. Introduction

[2] In the collisionless magnetospheric environment, wave-particle interactions can serve as a dominant mechanism for pitch angle scattering loss, energy diffusion, and anomalous cross-field transport and it has been suggested that very low frequency (VLF) whistler waves play an important role in scattering inner magnetospheric and radiation belt electrons [*Dungey*, 1963; *Kennel and Petschek*, 1966]. This contention is based both on the observational ubiquity of VLF whistlers in the region [*Gurnett and O'Brien*, 1964; *Dunckel and Helliwell*, 1969; *Sazhin and Hayakawa*, 1992], and the fact that such waves can resonate efficiently with electrons over a wide energy range [*Kennel and Petschek*, 1966; *Horne and Thorne*, 1998; *Summers et al.*, 1998].

[3] In recent years considerable attention has focused on VLF whistler waves that are observed in the outer radiation

[1]Institute of Geophysics and Planetary Physics, University of California, Los Angeles, California, USA.
[2]Department of Physics and Astronomy, University of California, Los Angeles, California, USA.
[3]JNL Scientific, Casa Grande, Arizona, USA.
[4]Astronomical Institute, ASCR, Prague, Czech Republic.
[5]Department of Space Physics, Institute of Atmospheric Physics, Prague, Czech Republic.
[6]Faculty of Mathematics and Physics, Charles University, Prague, Czech Republic.
[7]Southwest Research Institute, San Antonio, Texas, USA.
[8]Department of Physics and Astronomy, University of Iowa, Iowa City, Iowa, USA.
[9]Laboratory for Geospace Science, NASA Goddard Space Flight Center, Greenbelt, Maryland, USA.
[10]Mullard Space Science Laboratory, University College London, Holmbury St. Mary, UK.

0148-0227/10/2009JA014932

belt region between about 3 and 7 R_E (R_E is the Earth's radius = 6371 km). Pitch angle and energy diffusion rates of electrons due to the observed VLF whistler emissions have been calculated [e.g., *Horne et al.*, 2003] and the time scale for acceleration and flux enhancement of relativistic energies was found to be about 1 day, which is in good agreement with observations [*Horne et al.*, 2005]. Indeed, many studies indicate that whistler waves in the inner magnetosphere can accelerate electrons to MeV energies [*Horne*, 2007; *Omura et al.*, 2007; *Summers et al.*, 2007; *Albert et al.*, 2009; *Kasahara et al.*, 2009]. Also, based on observational coincidence, it has also been suggested that VLF whistler waves cause the loss of electrons in the form of microburst precipitation [*Lorentzen et al.*, 2001]. Studies such as these (and many others), reinforce the idea that whistler waves play a major role in electron scattering and acceleration in the radiation belt region.

[4] The goal here is to examine the basic generation mechanism of whistler waves observed in the outer radiation belt region, with this study being prompted by recent Cluster II satellite observations that include the measurement of high resolution electron distribution functions within the whistler wave source region [*Santolík et al.*, 2009; 2010]. In general, the source of whistler emissions is located in the equatorial region [*LeDocq et al.*, 1998; *Parrot et al.*, 2003a; *Santolík et al.*, 2004, 2005; *Santolík*, 2008], where the waves have been associated with anisotropic electron distributions [*Tsurutani et al.*, 1979]. The whistler waves in the radiation belt region are often observed in two distinct bands on the whistler wave branch, with the upper band referring to waves with frequency $0.5f_{ce} < f < f_{ce}$ (f_{ce} = equatorial electron gyrofrequency) and the lower band in the approximate frequency range $0.2f_{ce} < f < 0.5f_{ce}$, with a characteristic gap in the emissions at $0.5f_{ce}$ [*Tsurutani and Smith*, 1974; *Meredith et al.*, 2001, 2009]. Chorus is a class of whistler waves that are highly structured, bursty emissions within the upper and/or lower frequency band [*Dunckel and Helliwell*, 1969; *Tsurutani and Smith*, 1974, 1977; *Burtis and Helliwell*, 1975, 1976; *Santolík et al.*, 2003a]. Although chorus usually refers to structured, discrete wave packets within the whistler branch, there are observations of alternating time intervals of smooth, unstructured emissions and discrete chorus elements within the upper or lower frequency band [*Tsurutani et al.*, 2009; *Santolík et al.*, 2009, 2010]. The generation of the structured, discrete whistler mode chorus waves involves nonlinear processes and spatial inhomogeneities [e.g., *Nunn et al.*, 1997, 2009; *Omura et al.*, 2008, 2009], whereas the unstructured, smooth whistler emissions have been explained using linear and quasi-linear theory [e.g., *Hashimoto and Kimura*, 1981; *Cornilleau-Wehrlin et al.*, 1985; *Solomon et al.*, 1988]. The focus of the present study is on understanding the generation of an observed unstructured whistler emission and it is shown that a combination of linear and nonlinear processes can lead to both upper and lower band emissions of this type.

[5] The approach here makes use of recent high resolution Cluster observations of whistler waves in their source region and accompanying electron distribution functions to theoretically examine at its most basic level wave generation and the self-consistent effects on the particles. A companion paper by *Santolík et al.* [2010] discusses in detail the observations made on July 24, 2003 of a highly anisotropic electron distribution with perpendicular temperature 10 times the parallel temperature ($T_\perp/T_\parallel$ = 10), which was found concurrent with whistler emissions within their source region. The whistler wave emissions observed during this event were two-banded with components in both the lower ($0.2f_{ce} < f < 0.5f_{ce}$) and upper ($0.5f_{ce} < f < f_{ce}$) frequency bands, with the characteristic gap at $0.5f_{ce}$; the emissions in both bands were smooth and continuous with essentially no fine structure (e.g., no rising or falling tones). Our theoretical approach uses realistic parameters based on the observations, along with a newly developed two-dimensional (2D) electromagnetic (EM) particle in cell (PIC) code which uses the Darwin approximation. Linear theory shows that for the observed parameters of the July 24, 2003 event, whistler waves over a wide range of propagation angles are unstable, demanding the necessity of a 2D code, and in order to use realistic parameters in 2D, only an EM PIC code that employs the Darwin approximation is computationally feasible.

[6] The results from the theoretical study here shed important insight into the generation and effects of whistler waves for the July 24, 2003 event. For example, the observed distribution function is found to be linearly unstable to whistler waves in the upper band ($0.5f_{ce} < f < f_{ce}$), while lower band ($0.2f_{ce} < f < 0.5f_{ce}$) whistler waves are linearly stable. The PIC simulation, which highlights the limitations of linear theory, shows that nonlinear wave-wave coupling processes can lead to the excitation of the lower frequency band waves. These theoretical findings are in good agreement with observations for this event that show the presence of both lower and upper frequency band wave emissions. The simulation results also show that the instability saturates not only by a reduction of the temperature anisotropy that originally provides the free energy for the waves, but also due to heating of the cold background electrons, which increase in temperature by a factor of about 3. This result suggests a possible heating mechanism for cold plasma as it is transported into the magnetosphere from the plasmasphere in the dayside-afternoon sector. Another result of the simulations is that a high energy plateau forms on the hot electron parallel distribution function, which may drive additional instabilities.

[7] The paper is outlined as follows. In section 2 a brief summary of the waves and particles observed for the July 24, 2003 event is provided. In section 3 a linear theory study using the observed parameters described in section 2 is presented, followed by the particle in cell simulation study of the same event in section 4. Summary and conclusions finish the paper in section 5.

2. Observations

[8] On July 24, 2003, at about 01:24 UT, the Cluster 4 satellite crossed the magnetic equator at about 4.5 R_E radial distance on the afternoon sector (~15 MLT) and whistler wave emissions were observed. Wave data from the Wideband Data (WBD) instrument mounted onboard Cluster 4 is shown in Figure 1. Whistler mode waves can be seen as the two-banded emission above and below one-half the electron gyrofrequency ($0.5f_{ce}$ ~ 4.5 kHz) near the magnetic equator between about 01:14 UT to 01:28 UT, highlighted between the two vertical black lines. An analysis of the wave data

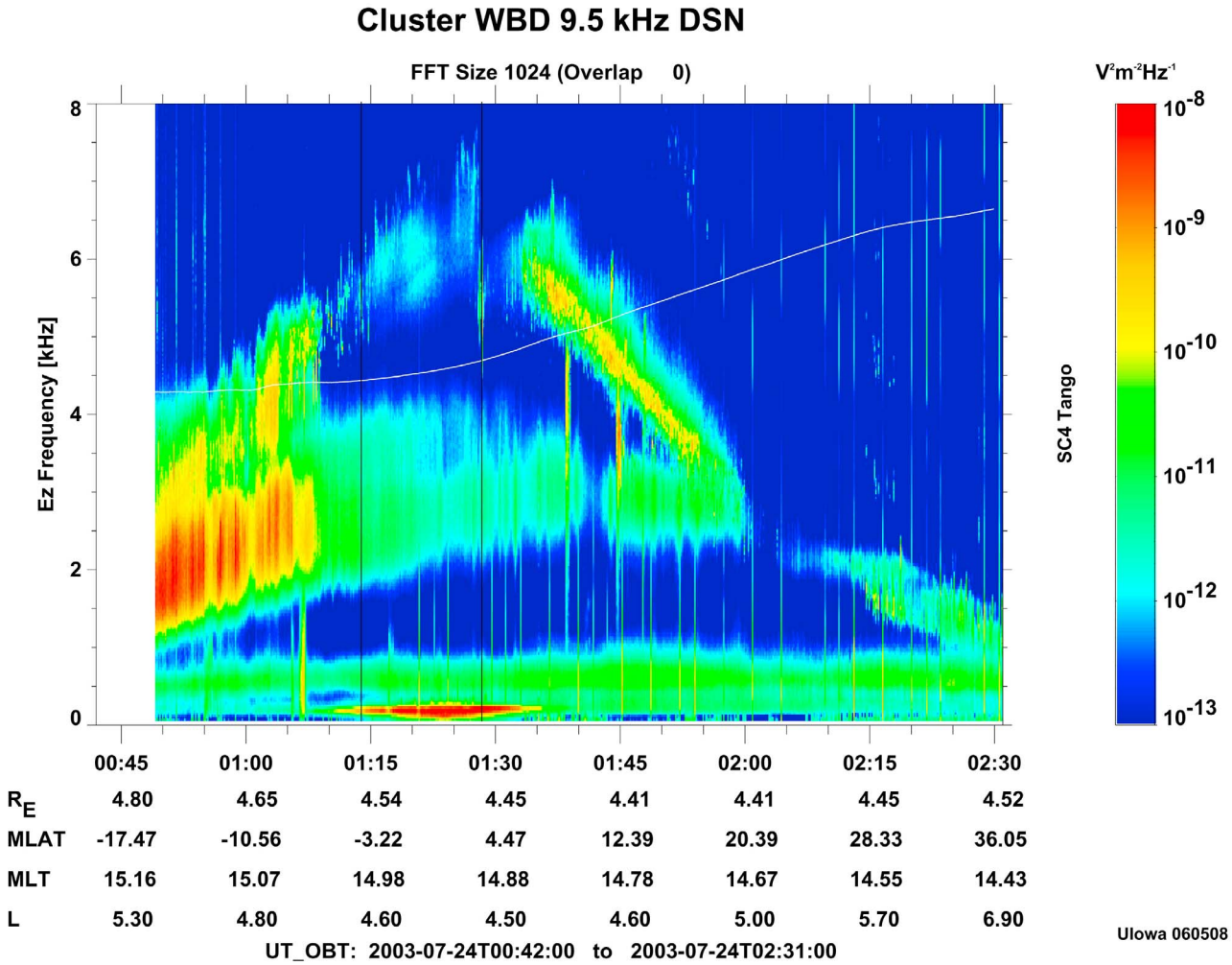

Figure 1. Electric field spectrogram is presented from the Wideband Data (WBD) instrument onboard the Cluster 4 satellite on July 24, 2003 showing frequency (in kHz) versus UT, color coded in electric field spectral intensity $(V/m)^2Hz^{-1}$ with red representing the most intense waves and blue the least intense. The white line starting at about 4.3 kHz at 00:50 UT shows the local value of one-half the electron gyrofrequency, $0.5f_{ce}$, which is based on the value of the ambient magnetic field at the satellite location.

from the STAFF instrument onboard Cluster has shown that during this event the satellite passed directly through the region where the whistler waves are generated. This analysis is described in a companion paper by *Santolík et al.* [2010], which discusses Cluster data from the event of July 24, 2003 in detail. Using techniques described by *Santolík et al.* [2003b], by examining data from STAFF, *Santolík et al.* [2010] were able to determine that Cluster 4 flew through the whistler wave source region at about 01:24 UT.

[9] In the whistler wave source region during the event on July 24, 2003, the properties of electrons have been examined using data from the Plasma Electron and Current Experiment (PEACE) instrument onboard Cluster 4. Figure 2 shows the electron energy spectrogram during the time interval during which Cluster crossed the magnetic equator and observed the whistler waves. Figure 2 shows velocity (in km/s) versus UT color coded in energy density for 90° pitch angles during the time interval highlighted by the black vertical lines in Figure 1. The black curve in Figure 2 shows the ambient magnetic field, B_o (scale on the right). The red bands show injections of electrons primarily transverse to B_o (similar plots at 0° and 180° do not show such strong enhancements) when the whistler mode emissions are observed. At the equatorial crossing within the wave source region, as indicated by the black vertical line at 01:24 UT, the most intense, highest velocity electron injections occur.

[10] The electron velocity space differential energy flux observed at ~01:24 UT when the whistler waves are generated is shown in Figure 3. The left panel shows high resolution wave data from WBD instrument and on the right panel the corresponding electron energy flux from PEACE is shown at the same time. The WBD wave data on the left panel shows the double banded whistler wave emission above about 2 kHz and below f_{ce} (~9 kHz), with the typically observed gap occurring at about 0.5 f_{ce} (~4.5 kHz). The lower band is centered just below 3 kHz, while the upper band is centered at about 6 kHz, and both bands are rather smooth and continuous, without any structured

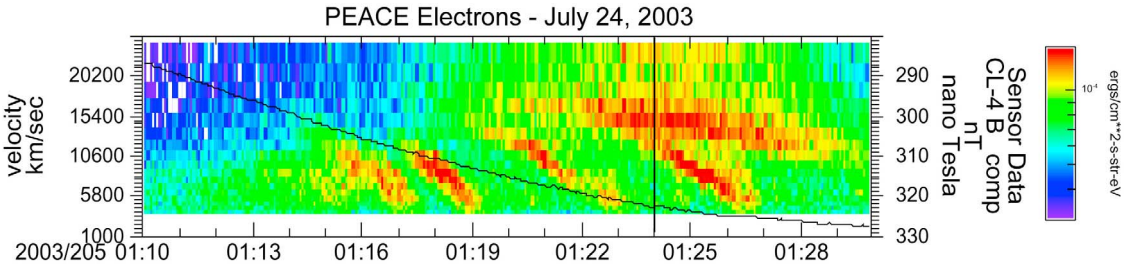

Figure 2. Electron velocity spectrogram (velocity in km/s versus UT) color coded in energy density is shown during the time interval highlighted between the two vertical black lines in Figure 1. The total magnetic field is shown by the black curve, with scale on the right. The black vertical line at 01:24 UT indicates when the whistler emissions were observed at their source in the near-equatorial region.

chorus-like features. The periodic structures in the upper band are satellite spin related and are not related to the rising-falling tone structures often observed in chorus. There are also intense whistler waves below 1 kHz, distinct from the higher frequency emissions, that are non-locally generated lower frequency waves (<0.2 f_{ce}) which are propagating toward the equator [*Santolík et al.*, 2009]; these wave are most likely magnetospherically reflected whistler mode chorus [*Parrot et al.*, 2003b, 2004; *Santolík et al.*, 2009] generated in another region. The PEACE electron data on the right panel shows the electron phase space density, with velocity transverse to the ambient magnetic field ($v_\perp$) plotted versus parallel velocity ($v_\parallel$), both in km/s, color coded in differential energy flux. A highly anisotropic component with perpendicular temperature ($T_\perp = 0.5mv_\perp^2$) about 10 times the parallel temperature ($T_\parallel = 0.5mv_\parallel^2$), i.e., $T_\perp/T_\parallel = 10$, can be seen at velocities below about 40,000 km/s. Also, a higher energy electron component can be seen near the upper velocity cutoff with energies ~10 keV. Further analysis shows that in addition to the anisotropic species with density $n \sim 0.5$ cm^{-3} and $T \sim 300$ eV, a cool ($T \sim 15$ eV), denser ($n \sim 2.5$ cm^{-3}) core electron component and an even colder (<5 eV), very dense ($n \sim 28$ cm^{-3}) were also present. These results have been found by fitting the electrons to a bi-Maxwellian distribution function to determine temperatures and densities [*Santolík et al.*, 2010]. The results from this analysis are compiled in Tables 1 and 2. The most important feature of the electrons is the population with the highly anisotropic distribution function, which can serve as a free energy source that can be unstable, leading to the generation of whistler waves (and possibly other waves) in the plasma. It is rare to observe such a highly unstable distribution function at the same time as the waves and a theoretical examination of these coupled observations is now carried out, starting with linear theory in the next section.

3. Linear Theory

[11] Using the observed electron distribution functions described in section 2, with parameters given in Table 2, a

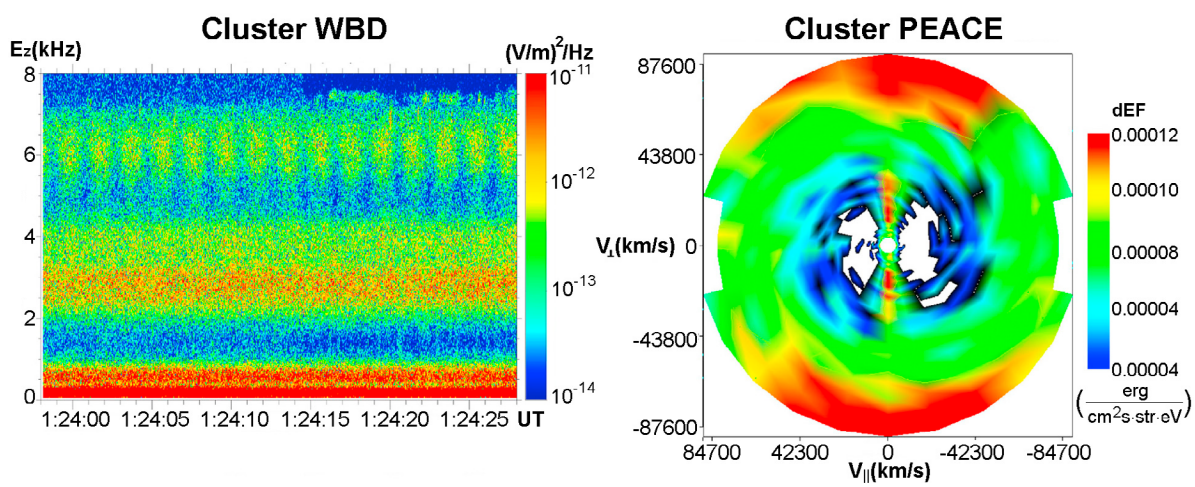

Figure 3. (left) Frequency spectrogram (kHz versus UT, color coded in electric field intensity) and (right) the differential electron energy flux in velocity space, with velocity perpendicular ($v_\perp$) to the ambient magnetic field plotted versus velocity parallel ($v_\parallel$) to the ambient magnetic field. In Figure 3 (left), the frequency spectrogram on the vertical axis ranges from 0 kHz to 8 kHz and the horizontal scale goes from 01:23:58 UT to 01:24:28 UT, color coded on a log scale with red representing the most intense waves at 10^{-11} (V/m)^{2}Hz^{-1} and blue the weakest at 10^{-14} (V/m)^{2}Hz^{-1}. In Figure 3 (right), the velocities are in km/s and the axes range is $\pm 8.76 \times 10^4$ km/s, color coded in differential energy flux (ergs/cm^{2}s · str) with red representing 0.000158 ergs/cm^{2}s · str and blue 4.17×10^{-5} ergs/cm^{2}s · str.

Table 1. A Summary of the Waves Observed by the WBD Instrument in the Source Region at 01:24 UT for the Event on July 24, 2003[a]

Wave Type	Frequency (kHz)	Frequency (f_{ce})
Lower band whistler waves	2–4	0.2–0.4
Upper band whistler waves	5–7	0.6–0.8

[a]The local electron gyrofrequency is taken to be f_{ce} = 9 kHz, based on magnetometer measurements made at the time.

linear theory study has been carried out using a modified version of the WHAMP linear dispersion solver [*Rönnmark*, 1982, 1985]. For this study, only two electron populations are included, the core and the mid-energy anisotropic electrons, using the values for density and temperature in Table 2; these two electron species hereafter are referred to as cold and hot electrons, respectively. The value of the electron cyclotron frequency to electron plasma frequency ratio used in this study is 0.587. The parameters for the high-energy population (>20 keV) in Table 2 are not well defined and this species is not included in the present study.

[12] For the given parameters, Figure 4 shows linear theory results in terms of growth rate γ, maximized over all wave numbers and angles, plotted versus frequency ω, both normalized to the electron gyrofrequency (Ω_e). The main result is that for the observed parameters, the anisotropy in the hot electron distribution function drives waves unstable with a frequency range between $0.55\Omega_e$ and $0.89\Omega_e$, on the whistler wave branch, with peak growth at frequency $\omega = 0.71\Omega_e$. The unstable range of frequencies corresponds to what is referred to as the upper band, which are wave emissions with frequencies greater than $0.5\Omega_e$.

[13] The angle at which the growth rate maximizes is oblique to the ambient magnetic field. This is illustrated in Figure 5, which shows growth rate γ normalized to Ω_e, maximized over all wave numbers and frequencies, versus propagation angle θ. Although wave growth occurs over a wide range of angles, peak growth is at 40.6°. Note that at less oblique propagation angles, i.e., <41°, the frequencies of the unstable waves tend to be on the higher frequency end of spectrum, i.e., $\omega > 0.71\Omega_e$, with parallel propagation ($\theta = 0°$) corresponding to a frequency $\omega = 0.89\Omega_e$, while the more oblique unstable waves near 55° have lower frequencies at about $0.6\Omega_e$. Note that at parallel propagation the growth rate is nonzero, but is about three orders of magnitude smaller than the maximum growth at 40.6° and is thus not visible on the (vertical) linear scale used in Figure 5. The results here are consistent with the linear theory results of temperature anisotropy driven oblique whistler waves

Table 2. Properties of the Electrons During the Whistler Wave Source Event Observed by the PEACE Instrument on July 24, 2003 at 01:24 UT

Electrons	Energy (eV)	$T_\perp/T_\parallel$	Density (cm^{-3})
cold	<5	1	28
core	15	1.5	2.5
mid-energy	300	10	0.5
high-energy	20,000	?	0.8 (?)

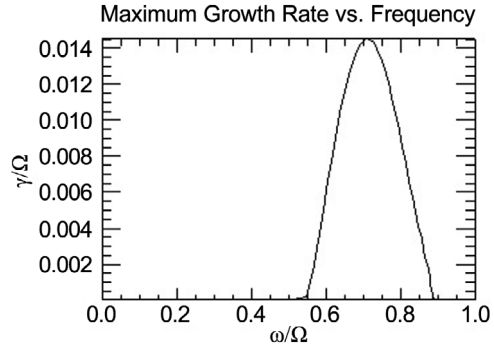

Figure 4. Linear theory dispersion relation results are shown using the WHAMP numerical dispersion solver with the electron parameters (see Table 2) for the whistler wave source event on July 24, 2003 at 01:24 UT. Growth rate γ, maximized over all wave numbers and angles, is plotted versus frequency (ω). Both frequency scales are normalized to the electron gyrofrequency (Ω_e).

excited above $0.5\Omega_e$ found by *Hashimoto and Kimura* [1981].

[14] Clearly the temperature anisotropy in the hot electron population provides the relatively large growth rate, which peaks at $\gamma = 0.014\Omega_e$ and real frequency $\omega = 0.71\Omega_e$ (see Figure 4). The wave number (k) of the maximum growing wave occurs at $k\rho_{ec} = 0.09$, $k\rho_{eh} = 0.23$, where ρ_{ec} and ρ_{eh} are the cold and hot electron gyroradii, respectively (not shown). As noted, peak growth occurs at an oblique angle of 40.6°, which for the parameters used in this study is where the bulk of the hot electrons are in gyroresonance with the waves. The resonance velocity $v_{R,}$ is given by:

$$v_R = \frac{\omega - \Omega_e}{k_\parallel} \tag{1}$$

and at 40.6°, $v_R = 1.6v_{th}$, where v_{th} is the thermal velocity of the hot (anisotropic) electrons. For propagation angles smaller or larger than 40.6°, the resonance velocity is larger than this value, e.g., for $\theta = 0°$, $v_R = 3.0v_{th}$ and for $\theta = 49°$,

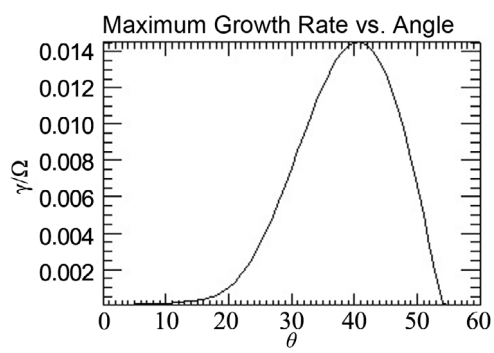

Figure 5. Linear theory dispersion results are shown using the electron distribution parameters for the whistler wave source event on July 24, 2003 at 01:24 UT with growth rate γ, maximized over all frequencies and wave numbers, plotted versus propagation angle θ. The growth rate is normalized to the electron gyrofrequency (Ω_e).

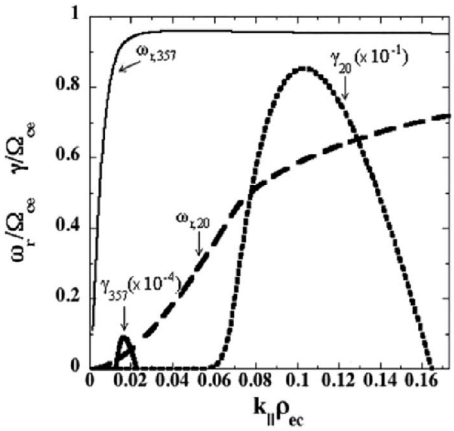

Figure 6. Linear dispersion relation (frequency or growth rate versus wave number) is shown for two different values of c/v_{te} = 20 and 357, with all other parameters being the same as discussed in section 3 and given in Table 2. Only the parallel propagation case (θ = 0°) is shown here. Both the real frequency and growth rate are normalized to the electron gyrofrequency, ω_r/Ω_e and γ/Ω_e, respectively. The real frequencies denoted as $\omega_{r,357}$ (thin solid line) and $\omega_{r,20}$ (long dashed line) correspond to c/v_{te} = 357 and 20, respectively. The growth rates denoted by γ_{357} (thick solid line) and γ_{20} (short dashed line) correspond to c/v_{te} = 357 and 20, respectively, with the corresponding multiplicative factor (in powers of 10) to be applied to number scale on the vertical axis to provide the actual numerical value for each growth rate. Parallel (θ = 0°) wave number times the cold electron gyroradius $k_{\|}\rho_{ec}$, is shown on the horizontal scale for all curves.

$v_R = 2.0v_{th}$ and thus the growth rates are correspondingly smaller at these angles.

4. Particle in Cell Simulations

[15] To examine the nonlinear aspects of the whistler instability discussed in the previous section, a particle in cell (PIC) simulation study has been carried out using the same observed parameters for the linear theory results discussed in section 3. A two-dimensional (2D), electromagnetic (EM), particle in cell (PIC) simulation code that employs the Darwin approximation [*Darwin*, 1920] is used here. This code has been developed as part of the UPIC framework described in *Decyk* [2007]. Most EM PIC codes solve the full set of Maxwell's equations self-consistently with the Lorentz force equation used to push electrons and ions through the simulation system [e.g., *Dawson*, 1983]. The Darwin EM PIC model neglects the transverse component of the displacement current (but keeps the longitudinal part) in the full set of Maxwell's equations, which makes them radiation-free, but leaves the whistler physics unaffected from its fully electromagnetic counterpart [*Busnardo-Neto et al.*, 1977; *Hewett*, 1985; *Geary et al.*, 1986]. The Darwin approximation becomes useful since the observed speed of light to thermal velocity ratio (c/v_{te}) for the July 24, 2003 event is c/v_{te} = 357, which in a full EM PIC code would require an unreasonably small time step in order to resolve the light wave branch. Typically full EM PIC codes use values of c/v_{te} = 20. The advantage of the Darwin model is that one can use a time step which is set by the greater of the electron plasma frequency or the electron gyrofrequency, instead of the speed of light. This allows the realistic value of c/v_{te} = 357 to be retained, which is important because the value of c/v_{te} used strongly affects the dispersion relation.

[16] The necessity of using a realistic value for c/v_{te} is illustrated in Figure 6, which compares the linear theory with all of the same parameters as discussed in Section 3 and Table 2, except with two different values used for c/v_{te} (=20 and 357). For comparison purposes, only the parallel propagation case (θ = 0°) is shown. The two different values for c/v_{te} give entirely different results for the unstable range of frequencies and wave numbers, as well as for the growth rate, which differ by 3 orders of magnitude. Large differences in frequencies, wave numbers and growth rate are also found at oblique angles of propagation when the different values of c/v_{te} are used. The result of Figure 6 emphasizes the necessity for using the 2D EM Darwin PIC code in order to maintain realistic parameters to study the event on July 24, 2003.

[17] Results from the 2.5D EM PIC Darwin code using the identical parameters from the linear theory discussed in Section 3 and provided in Table 2 are now discussed. Note that the 2.5D refers to the simulation having 2 spatial dimensions and 3 velocity dimensions. The system is doubly periodic in x and y using 1024 × 1024 grids, with the grid length in both dimensions equal to the cold electron Debye length, i.e., $\Delta x = \Delta y = \lambda_{Dec}$, and a total (cold + hot) of 3.145850 × 10^7 particles. The ambient magnetic field is aligned along the x simulation axis. All distribution functions are modeled initially as bi-Maxwellian, with the cold electrons isotropic ($T_{\perp ec}/T_{\|ec}$ = 1) and the hot electrons anisotropic ($T_{\perp eh}/T_{\|eh}$ = 10). Since we are interested here in relatively high frequency electron-mode whistler waves with times that scale to the electron gyrofrequency, ions, which over the course of a full simulation run would complete less than 2 gyroperiods, are treated as an immobile, charge neutralizing background.

[18] As expected, the anisotropic electrons drive instabilities and this can be seen in Figure 7, which shows the time history of the (normalized) electromagnetic (EM) field energy on the left panel and the (normalized) electrostatic (ES) electric field energy on the right panel. Wave field energy for both the EM and ES waves peaks at about $t = 900\Omega_e^{-1}$ with the total field energy values for both EM and ES waves falling to about 40 times the simulation thermal noise level (not shown) by the end of the simulation run, i.e., at $t = 3600\Omega_e^{-1}$ (Ω_e^{-1} is the inverse electron cyclotron frequency).

[19] A wave spectral analysis for the EM waves is shown in Figure 8 with the integrated (normalized) magnetic vector potential plotted versus frequency. The background noise level from a simulation run with the temperature anisotropy removed but all other parameters the same is shown by the dashed line for reference. There is very good correspondence with linear theory in terms of the waves excited in the frequency band above $0.5\Omega_e$, with peak wave power occurring at ω = 0.65 to $0.70\Omega_e$ at propagation angles of 39° to 41° and wave numbers $k\rho_{ec}$ = 0.07 to 0.08. The growth rate for these modes has been calculated to be

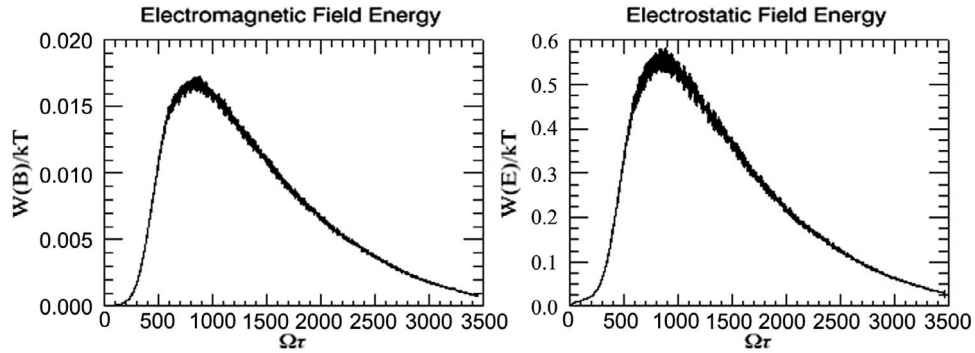

Figure 7. Results from the 2.5D EM Darwin PIC simulation run are shown with the time history of the electromagnetic field energy on the left panel and the electrostatic field energy on the right panel. The field energies are normalized to the thermal energy and the horizontal axis on both panels is given in units of electron cyclotron frequency multiplied by time, i.e., $\Omega_e t$. The parameters used for the PIC simulation are identical to the parameters used in the linear theory study.

$\gamma \sim 0.012\Omega_e - 0.014\Omega_e$. The agreement with linear theory for the whistler wave upper frequency band is excellent keeping in mind that the finite grid system in the simulation reduces the resolution of possible wave propagation angles and wave numbers.

[20] An unexpected result seen in Figure 8 is the presence of waves at lower frequencies below $0.5\Omega_e$, ranging approximately between ~$0.1\Omega_e$ and ~$0.4\Omega_e$, which are initially stable according to linear theory as seen in Figure 4. These lower band wave modes have wave power more than an order of magnitude greater than the noise level. A detailed analysis shows that the lower frequency wave modes below $0.5\Omega_e$ are nonlinearly excited by wave-wave coupling between two different wave modes of the unstable spectrum which transfers power to a third wave [e.g., W*eiland and Wilhelmsson*, 1976]. In wave-wave coupling, the frequencies (ω_3) and wave numbers ($\mathbf{k}_3$) of the product wave modes which can become enhanced must satisfy the following matching conditions:

$$\omega_3 = \omega_1 \pm \omega_2 \tag{2}$$

$$\mathbf{k}_3 = \mathbf{k}_1 \pm \mathbf{k}_2 \tag{3}$$

where the indices 1 and 2 correspond to the two interacting waves. Note that this is a multidimensional set of equations whereby forward and backward propagating waves at different angles can interact and satisfy these matching equations. A detailed analysis shows that the upper frequency band whistler waves which are generated over a fairly broad frequency and wave number spectrum can interact with each other leading to enhanced power in the lower frequency band wave modes. An example of this is illustrated in Figure 9, which shows the time history and power spectrum of three individual wave modes from the simulation, whereby the first two parent modes (top two set of panels) interact and satisfy the matching conditions in equations (2) and (3) using the negative sign, which leads to an enhancement of the third daughter mode shown by the panels at the bottom. Looking at the time history of each mode, it can be seen in Figure 9 that the daughter mode (bottom panel) gains wave energy when $t > 700\Omega_e^{-1}$, which is after first two modes have achieved significant wave power via the linear anisotropy instability and then interact. Table 3 shows the set of wave modes in the simulation that interact and by using the negative sign in equations (2) and (3) produce the enhanced power in three different lower frequency band wave modes. It should be kept in mind that the finite resolution grid used in the simulation produces three distinct modes in the lower band with increased wave power, but it is expected that the lower band enhancement would be more continuous in frequency and wave number using a higher resolution system that would allow more wave modes to interact.

[21] It is interesting to note that the parent modes seen in Table 3 and Figure 9 propagate at different angles and

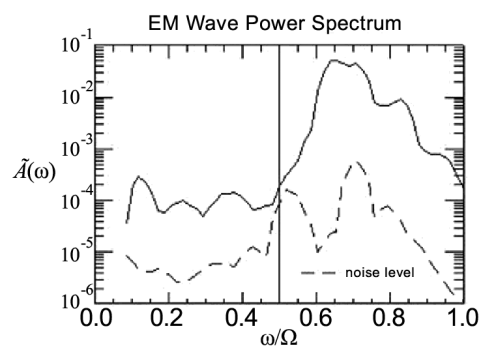

Figure 8. A wave power spectral analysis from the 2.5 EM Darwin PIC simulation run (wave energy time histories in Figure 7) is presented with the Fourier transformed, integrated magnetic vector potential over all wave modes (power) plotted versus frequency (normalized to the electron gyrofrequency Ω_e). The dashed line shows the wave power spectrum from a simulation run when the free energy source (temperature anisotropy) is not included, with all other parameter beings the same, providing the background noise level for comparison. The vector potential is normalized such that $\tilde{A}(\omega) = qA(\omega)/mc\omega_{pe}\Omega_e$. A vertical straight line has been drawn to delineate half the electron gyrofrequency, i.e., $\omega/\Omega_{ce} = 0.5$; frequencies above this value are termed the upper frequency band and frequencies below $0.5\Omega_{ce}$ are considered the lower frequency band.

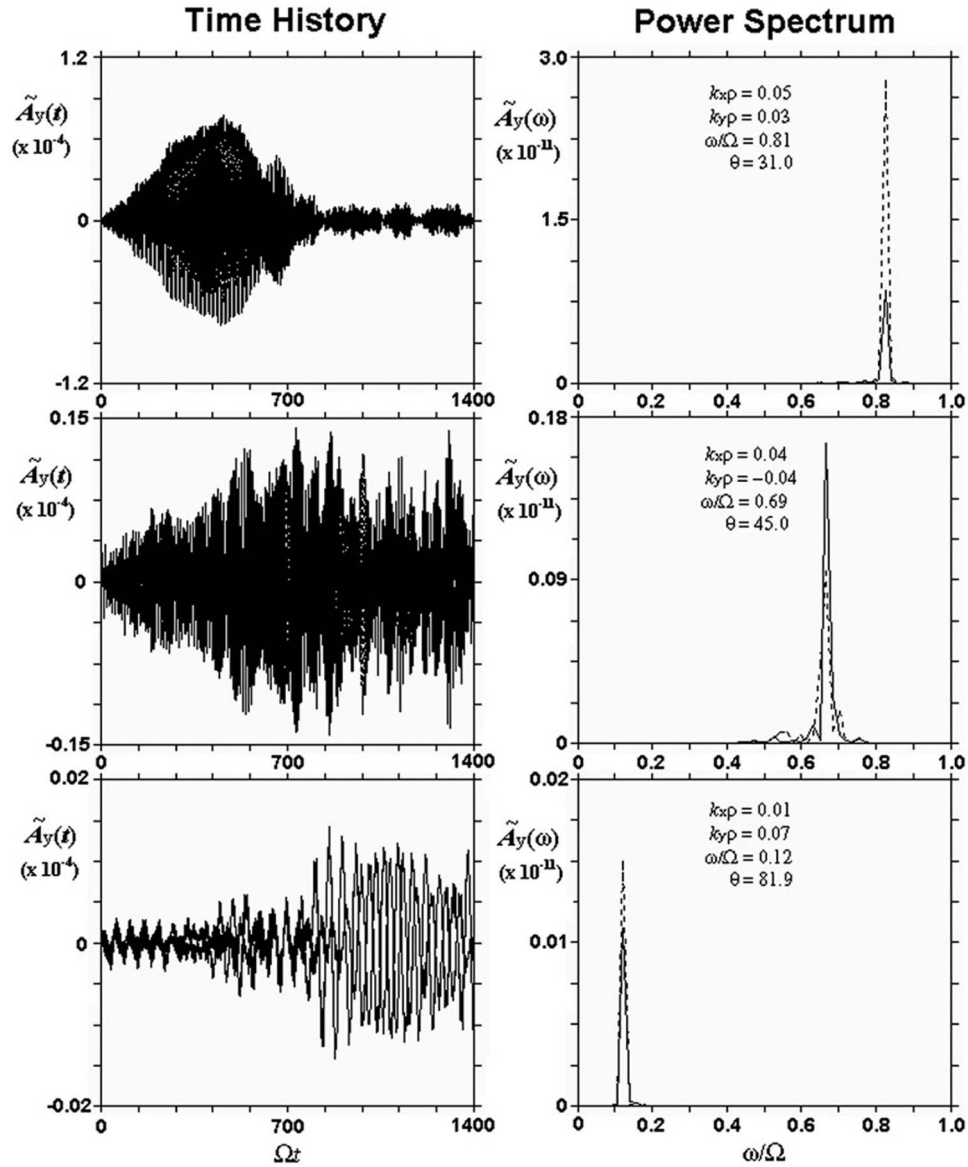

Figure 9. (left) The time history of the magnetic vector potential y component, $\tilde{A}_y(t)$ versus time ($\Omega_e t$), and (right) a power spectral Fourier analysis, $\tilde{A}_y(\omega)$ versus frequency (ω/Ω_e), is shown for three different wave modes from the simulation. (top and middle) The wave modes interact and satisfy the matching conditions given by equations (2) and (3) such that (bottom) the third wave mode is excited by nonlinear wave-wave coupling. Wave number, frequency, and propagation angle information are given in Figure 9 (right) for each mode.

produce a third mode which is more oblique than the two parent modes. This general trend such that wave modes become more oblique can be seen in Figure 10, which shows contours of magnetic wave power in k space up to $t = 900\Omega_e^{-1}$ on the left panel and for the entire simulation runup to $t = 3600\Omega_e^{-1}$ on the right panel. Figure 10 shows that early in the simulation run during the linear unstable phase, waves are excited most strongly at angles <45° as seen in the left panel (red regions below the diagonal line), while later in the run (right panel), wave power shifts to more oblique, lower frequency waves (red, aqua blue regions above the diagonal line) through the wave-wave coupling discussed above.

[22] The time history of the temperature for the cold and hot electron populations is presented in Figure 11. For each population, both the parallel (red) and perpendicular (green) temperature components are shown. The initially anisotropic hot electrons (right panel) show a decrease in the perpendicular temperature and an increase in the parallel temperature with time. The instability grows at the expense of the temperature anisotropy ($T_\perp > T_\parallel$) in the hot electrons and as a result of this wave growth, ensuing wave-particle interactions between the whistler waves and the hot electrons occur that alleviate this anisotropy such that the perpendicular temperature decreases and parallel temperature increases as indicated on the right panel of Figure 11. For

Table 3. A Detailed Listing of Wave Mode Data From the Simulation Run That Satisfies the Wave-Wave Coupling Equations (2) and (3)[a]

	Parent Mode 1	Parent Mode 2	Daughter Mode 3
ω/Ω_e	0.81	0.69	0.12
$k_x\rho_{ec}$	0.053	0.032	0.011
$k_y\rho_{ec}$	0.042	−0.042	0.074
ω/Ω_e	0.90	0.66	0.24
$k_x\rho_{ec}$	0.043	0.064	−0.021
$k_y\rho_{ec}$	0.011	−0.064	0.074
ω/Ω_e	0.95	0.71	0.35
$k_x\rho_{ec}$	0.032	0.064	−0.032
$k_y\rho_{ec}$	0.0	−0.032	0.032

[a]For each case, if the negative sign is taken in equations (2) and (3) for each respective quantity (frequency or wave number shown in the first column), i.e., if parent mode 2 (third column) is subtracted from parent mode 1 (second column), this matches almost exactly the values for these quantities of the daughter mode 3 taken from the simulation (fourth column). Note that all of the values in this table are taken from the simulations.

the cold electrons, as shown in the left panel of Figure 11, heating occurs in both the parallel and perpendicular directions, however, initially there is more perpendicular heating than parallel such that the cold electrons develop a mild anisotropy of their own. After about $t = 900\Omega_e^{-1}$, which coincides approximately with when the initial linear instability saturates, both the parallel and perpendicular components of the cold electron temperature continue to heat uniformly at about the same rate, reaching a temperature about 3 times the initial temperature. Electromagnetic trapping of the cold electrons by the unstable whistler waves is the likely acceleration mechanism [*Le Quéau and Roux*, 1987]. From the simulations, the resonance velocity of the fastest growing and largest amplitude whistler wave mode is found to be $v_R = 3.1v_{tc}$, which would allow a resonant interaction between the waves and the higher energy end of the cold electron distribution, ultimately resulting in heating of the cold population as found in Figure 11.

[23] The temperature anisotropy time history of the hot and cold electrons is shown in Figure 12. It can be seen that the hot electron anisotropy decreases as the wave energy increases due to the whistler instability, going from its initial value of $(T_\perp/T_\parallel)_{hot} = 10$ to $(T_\perp/T_\parallel)_{hot} = 2.6$ at the end of the simulation run ($t_{end} = 3600\Omega_e^{-1}$). The hot electrons remain anisotropic even though the instability saturates by $t \sim 900\Omega_e^{-1}$, indicating that it is the reduction of the anisotropy coupled with cold electron heating (as seen in Figure 11) that quenches the instability. It can be seen in Figure 12 that the cold electrons, which initially were isotropic with $(T_\perp/T_\parallel)_{cold} = 1$, acquire a weak anisotropy that peaks at $(T_\perp/T_\parallel)_{cold} = 1.3$ at $t \sim 1100\Omega_e^{-1}$.

[24] The result of the whistler instability as seen in Figure 12 is a reduction of the temperature anisotropy which occurs primarily through pitch angle scattering from perpendicular to parallel velocities. This can be seen in Figure 13, which shows hot electron velocity space contours (perpendicular velocity versus parallel velocity normalized to the cold electron thermal speed) at the beginning (Figure 13 (left)) and end (Figure 13 (right)) of the simulation run. The highly anisotropic distribution is seen by the elongated contour lines in perpendicular velocity at the beginning of the run (Figure 13 (left)) and by the end of the simulation the bulk of the distribution becomes nearly isotropic as seen by the more circular contours at lower velocities (Figure 13 (right)); note that at the end of the run the distribution is still somewhat elongated in the perpendicular direction.

[25] As can be seen in Figure 11 (right), along with the decrease in perpendicular temperature for the hot electrons,

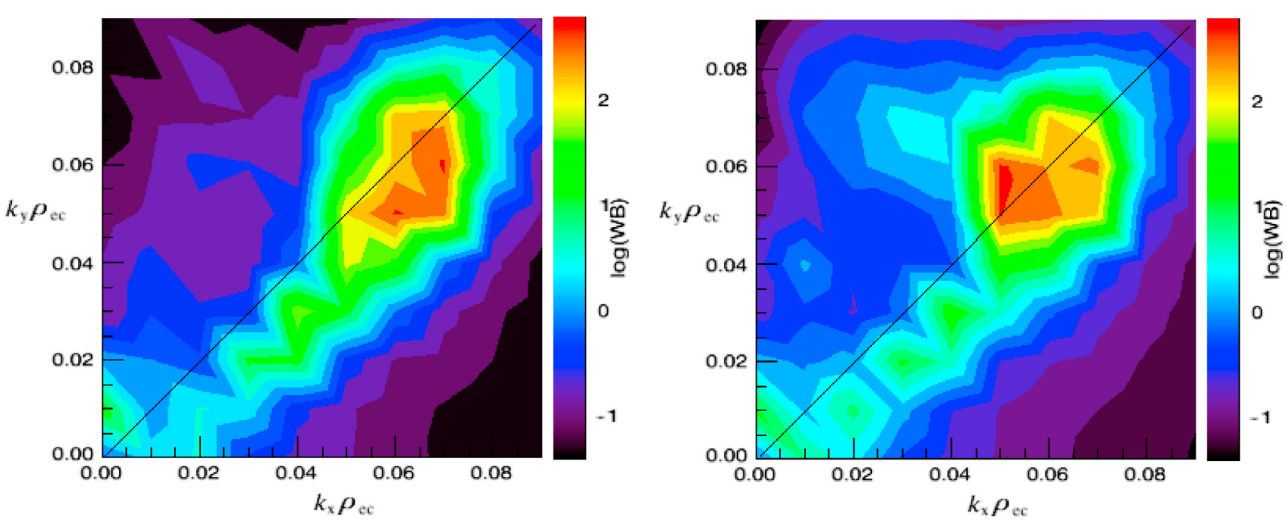

Figure 10. Magnetic wave power color contours are shown in k space (k_x versus k_y), where k_x is the wave number parallel to the ambient magnetic field (horizontal axis) and k_y is the wave number transverse to the ambient magnetic field (vertical axis). The diagonal line is drawn at $k_x = k_y$ and represents 45° wave propagation angle. The magnetic wave power is shown on a log scale with red representing the most powerful waves. (left) Results from the simulation runup to $t = 900\ \Omega_e^{-1}$ and (right) results from the entire simulation runup to $t = 3600\ \Omega_e^{-1}$.

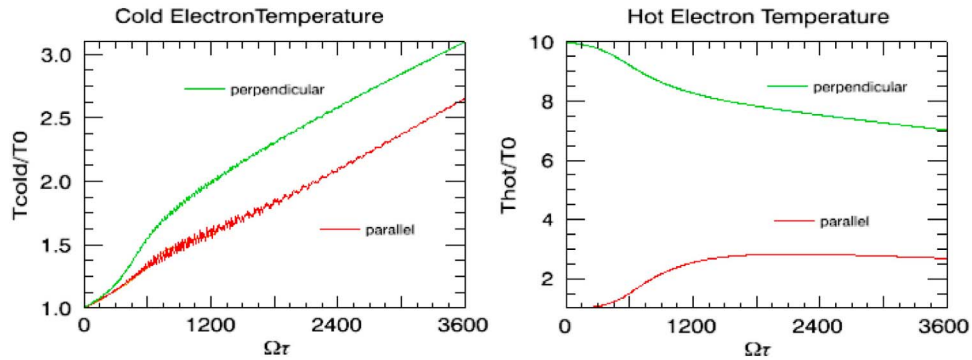

Figure 11. Temperature time histories are shown (left) for the cold electrons and (right) for the hot electrons from the simulation run. The parallel component of the temperatures is shown for each population by the red curve and perpendicular temperature by the green curve. For each plot the temperature is normalized to the initial parallel temperature of that species and on the horizontal scale time is multiplied by electron cyclotron frequency.

there is an increase in the parallel temperature. Although not readily apparent in Figure 13, the increase in parallel temperature of the hot electrons is due primarily to the formation of a high energy tail in the parallel distribution function. This can be seen more clearly in Figure 14, which shows the hot electron velocity distribution at three different times for both the parallel (Figure 14 (left)) and perpendicular (Figure 14 (right)) components. It can be seen clearly in Figure 14 (left) that for the parallel distribution function, wave-particle interactions lead to the formation of a significant high energy tail by the end of the simulation run (red curve), with a somewhat extended plateau whereby the highest energy electrons reach velocities up to ~20 times the initial cold electron thermal velocity. The Landau resonance velocity for the excited whistler waves, i.e., $\omega/k_{\|}$ (including the lower frequency band waves), ranges from $\pm(8 \text{ to } 15)v_{tc}$, which can cause high energy tail formation and a plateau in the parallel hot electron distribution that initially reached $\sim 9v_{tc}$ at $t = 0$ in the simulation A velocity distribution function with an extended, asymmetric plateau-like high energy tail like that seen in Figure 14, could drive the "fan" instability [*Kadomtsev and Pogutse*, 1967; *Shapiro and Schevchenko*, 1968; *Omelchenko et al.*, 1994], leading to the excitation of oblique waves with frequencies between the lower hybrid frequency and electron gyrofrequency; such a mechanism has been proposed for generating magnetospheric VLF whistler waves at $\sim 0.25f_{ce}$ [*Bošková et al.*, 1992]. Although the hot electron parallel distribution function is asymmetric, a calculation of the cyclotron resonant velocities given by equation (1) necessary for this mode to be unstable are too high, with $v_R > 20\ v_{tc}$, making it unlikely that the fan instability is active in this particular situation. The hot electron perpendicular distribution function in Figure 14 (right) shows that there is a rather significant bulk cooling whereby the distribution function narrows with the distribution peak increasing at lower velocities; the very high energy portion of the perpendicular distribution is relatively unaffected during the simulation run. The cold electron distribution functions (not shown) indicate that the wave-particle interactions result in bulk heating of the cold electrons in both the parallel and perpendicular directions and the cold distributions do not exhibit a high-energy plateau as seen in the parallel component of the hot electrons.

5. Conclusions

[26] On July 24, 2003 at 01:24 UT, the Cluster 4 satellite observed whistler wave emissions within their source region when crossing the magnetic equator on the dayside afternoon sector (~15 MLT) at about 4.5 R_E radial distance from the Earth. This fortuitous observation of whistler waves in their generation region, along with high resolution particle data that showed a highly anisotropic distribution concurrent with the waves, has been used with linear theory and a two-dimensional electromagnetic Darwin particle in cell simulation in order to gain insight into how the waves are generated and what nonlinear effects the waves have on the particles in terms of acceleration and energization.

[27] Linear theory shows that the observed hot anisotropic distribution function is unstable to oblique whistler waves with a frequency range between $0.55f_{ce}$ and $0.89f_{ce}$ (where f_{ce} is the electron cyclotron frequency), which would be considered the upper frequency band, i.e., frequencies

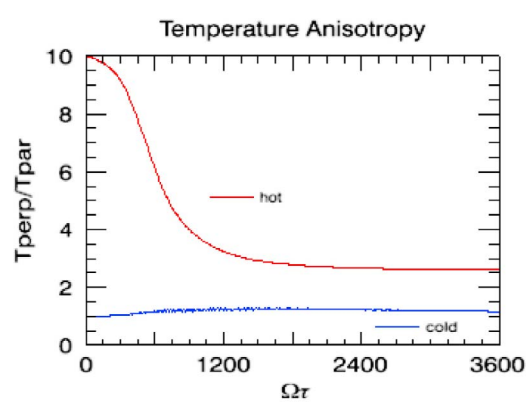

Figure 12. The simulation time history of the temperature anisotropy, which here is given by the perpendicular temperature over parallel temperature ($T_{\perp}/T_{\|}$), is shown for the hot electron population in red and the cold electron population in blue.

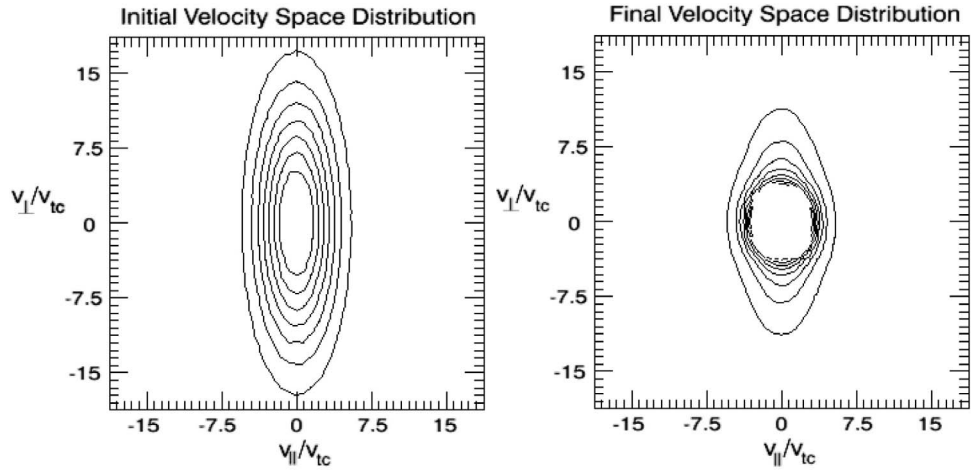

Figure 13. Velocity space contours for the hot electrons are shown with perpendicular velocity normalized to the initial background cold electron thermal speed ($v_\perp/v_{tc}$) plotted versus parallel velocity ($v_\parallel/v_{tc}$), (left) at the start of the simulation run and (right) at the end (t = 3600 Ω_e^{-1}) of the simulation run.

>0.5 f_{ce}. The numerical simulations confirmed the linear theory results showing whistler wave generation at the same range of upper band frequencies, but in addition showed that due to nonlinear wave-wave coupling, waves were also generated in the frequency range between $0.1f_{ce}$ and $0.4f_{ce}$, which is considered as the lower frequency band, i.e., frequencies <0.5 f_{ce}. For the parameters of this event, wave-wave coupling between waves within the linearly excited whistler spectra leads to the generation of the lower band whistler emissions. High resolution electric field data from the WBD instrument (Figure 3 (left)) shows a two-banded wave structure observed in the source region, in reasonable agreement with the frequency ranges found in the simulation wave power spectrum (Figure 8).

[28] The simulations show that the instability saturates by a combination of a reduction of the (driving) temperature anisotropy in the hotter electron distribution and heating of the cold electrons. As the cold electrons interact with the waves and are resonantly heated, they develop a mild temperature anisotropy, with $(T_\perp/T_\parallel)_{cold}$ ~ 1.3. This is notable since the PEACE instrument showed that the core electrons were observed to have a temperature anisotropy with $(T_\perp/T_\parallel)_{cold}$ = 1.5 (see Table 2). Another result of the wave-particle interactions is the formation of a high energy plateau in the hot electron parallel velocity distribution function. Such distributions may be related to flattened phase space distributions observed in the inner magnetosphere associated with whistler waves [*Li et al.*, 2010].

[29] There is quite reasonable agreement between observations and theory for this event which raises issues concerning the implications of the results. One issue is the persistence of the high degree of anisotropy in the hot electron distribution observed by the PEACE instrument onboard Cluster 4. It takes several seconds to measure a distribution function, e.g., ~16 s for the observation shown in Figure 3 (right), however the simulations show that the instability saturates within ~0.1 s, during which the anisotropy ($T_\perp/T_\parallel$) goes from 10 to 2.6. This implies that in order

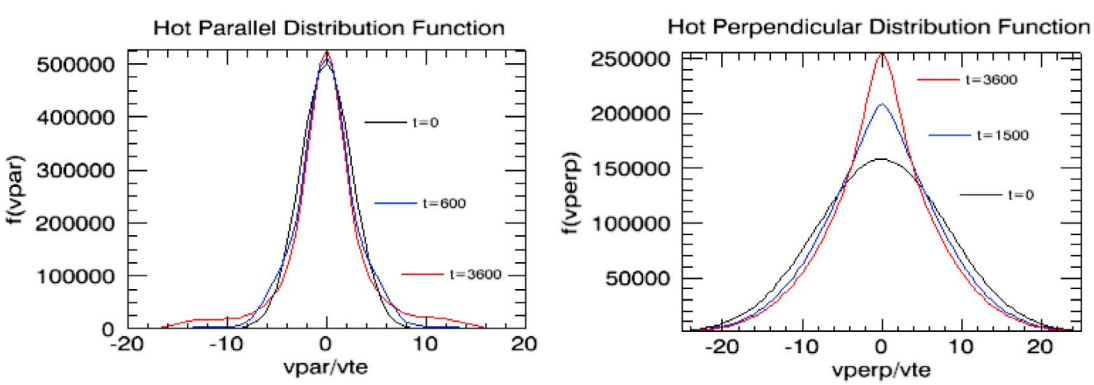

Figure 14. Velocity distribution functions are shown for (left) the hot electrons with the parallel distribution function and (right) the perpendicular distribution function. Distribution functions are shown at three different times during the simulation run with the black curve showing the initial distribution at t = 0Ω_e^{-1}, the blue curve at t = 600Ω_e^{-1} (parallel, Figure 14 (left)) and t = 1500Ω_e^{-1} (perpendicular, Figure 14 (right)), and the red curve showing the final distribution at the end of simulation run (t = 3600Ω_e^{-1}). Velocities (horizontal scale) for both panels are normalized to the initial cold electron thermal velocity.

to be observed within the instrument time resolution, the hot, highly anisotropic electrons are constantly being refreshed on time scales on the order of a tenth of a second. Recall that the observations for this event on July 24, 2003 were made in the dayside afternoon sector, presumably eliminating direct magnetotail convection as a source; thus it is not clear where the injection source is for such highly anisotropic distributions or what mechanism is maintaining the large anisotropy. Another issue is the heating of the cold electrons, which in the simulations showed a temperature increase of a factor of about 3 times the initial temperature. This cold plasma is presumably of plasmaspheric origin as it is transported from the inner to the outer magnetosphere in the dayside-afternoon sector [*Chen and Wolf*, 1972; *Chappell*, 1974; *Ober et al.*, 1998] and heating of this cool plasma by wave-particle interactions as found here represents a possible energization source that can affect large-scale plasmaspheric transport.

[30] Since only a single event is examined here, general conclusions in terms of whistler mode generation in the inner magnetospheric region are limited. Whistler waves are observed throughout the nightside-dawn-afternoon sector and have a variety of characteristics. For example, the event discussed here is for a rather smooth continuous spectrum that is double-banded, i.e., waves are observed above and below $0.5f_{ce}$, with a gap at $0.5f_{ce}$. But as is well documented in many observational studies, whistler mode chorus is often characterized by a high degree of structure in the frequency-time domain, with rising tones or falling tones being observed, which is not the case for this event. Such structure is likely due to nonlinear effects in the global magnetic field inhomogeneity [*Omura et al.*, 2008, 2009; *Shklyar and Matsumoto*, 2009], which is beyond the scope of the present, localized study. Also, whistler wave observations sometimes show only the upper band or only the lower band emissions, rather than both being observed at the same time as for the event discussed here. It is likely that the appearance of the different types of whistler wave frequency bands are caused by features in the driving distribution function, e.g., anisotropies and/or beams, and other parameters that affect the wave dispersion and instability properties, such as the temperatures and densities of the cold and hot electron species. A future goal is to find other source events with different types of whistler wave spectra in order to understand how they are generated and what effects the waves have on the particles in those cases.

[31] For many years space physics investigators examining plasma waves of various types have looked for the smoking gun in terms of wave generation, i.e., observed distribution functions that are unstable to an observed wave spectrum. The event discussed here is very close to being such an event and offers a rare opportunity, at least for this one case, to examine at ground zero the detailed physics involved with wave generation and wave-particle interactions in space plasmas.

[32] **Acknowledgments.** The authors wish to thank R. Richard for useful comments concerning this study. This work was supported by NASA GI grant NNX08AF26G and a NASA GSFC grant NNX07AJ86G. Work at the University of Iowa was carried out under NASA GSFC grant NNX07AI24G. O.S. acknowledges the support of grant KONTAKT ME842. Computing was carried out on the NAS SGI Altix machine as part of the Columbia supercomputing system and the NSF NCAR Frost Blue Gene supercomputing system.

[33] Zuyin Pu thanks David Nunn and another reviewer for their assistance in evaluating this paper.

References

Albert, J. M., N. P. Meredith, and R. B. Horne (2009), Three-dimensional diffusion simulation of outer radiation belt electrons during the 9 October 1990 storm, *J. Geophys. Res.*, *114*, A09214, doi:10.1029/2009JA014336.

Bošková, J., P. Triska, Y. A. Omelchenko, V. D. Shapiro, and V. I. Sotnikov (1992), The "fan" instability as a possible generating mechanism of VLF quarter-gyrofrequency emissions during the recovery phase of a magnetosopheric storm, *Stud. Geophys. Geod.*, *36*, 177, doi:10.1007/BF01614129.

Burtis, W. J., and R. A. Helliwell (1975), Magnetospheric chorus: Amplitude and growth rate, *J. Geophys. Res.*, *80*, 3265, doi:10.1029/JA080i022p03265.

Burtis, W. J., and R. A. Helliwell (1976), Magnetospheric chorus: Occurrence patterns and normalized frequency, *Planet. Space Sci.*, *24*, 1007, doi:10.1016/0032-0633(76)90119-7.

Busnardo-Neto, J., P. L. Pritchett, A. T. Lin, and J. M. Dawson (1977), A self-consistent magnetostatic particle code for numerical simulation of plasmas, *J. Comput. Phys.*, *23*, 300, doi:10.1016/0021-9991(77)90096-1.

Chappell, C. R. (1974), Detached plasma regions in the magnetosphere, *J. Geophys. Res.*, *79*, 1861, doi:10.1029/JA079i013p01861.

Chen, A. J., and R. A. Wolf (1972), Effects on the plasmasphere of a time-varying convection electric field, *Planet. Space Sci.*, *20*, 483, doi:10.1016/0032-0633(72)90080-3.

Cornilleau-Wehrlin, N., J. Solomon, A. Korth, and G. Kremser (1985), Experimental study of the relationship between energetic electrons and ELF waves observed on board GEOS: A support to quasi-linear theory, *J. Geophys. Res.*, *90*, 4141, doi:10.1029/JA090iA05p04141.

Darwin, C. G. (1920), The dynamical motions of charged particles, *Philos. Mag.*, *39*, 537.

Dawson, J. M. (1983), Particle simulation of plasmas, *Rev. Mod. Phys.*, *55*, 403, doi:10.1103/RevModPhys.55.403.

Decyk, V. K. (2007), UPIC: A framework for massively parallel particle-in-cell codes, *Comput. Phys. Commun.*, *177*, 95, doi:10.1016/j.cpc.2007.02.092.

Dunckel, N., and R. A. Helliwell (1969), Whistler-mode emissions on the OGO 1 satellite, *J. Geophys. Res.*, *74*, 6371, doi:10.1029/JA074i026p06371.

Dungey, J. W. (1963), Loss of Van Allen electrons due to whistlers, *Planet. Space Sci.*, *11*, 591, doi:10.1016/0032-0633(63)90166-1.

Geary, J. L., T. Tajima, J.-N. Leboeuf, E. G. Zaidman, and J. H. Han (1986), Two- and three-dimensional magnetoinductive particle codes with guiding center electron motion, *Comput. Phys. Commun.*, *42*, 313, doi:10.1016/0010-4655(86)90002-0.

Gurnett, D. A., and B. J. O'Brien (1964), High-latitude geophysical studies with satellite Injun 3 5. Very low frequency electromagnetic radiation, *J. Geophys. Res.*, *69*, 65, doi:10.1029/JZ069i001p00065.

Hashimoto, K., and I. Kimura (1981), A generation mechanism of narrow band hiss emissions above one half the electron cyclotron frequency in the outer magnetosphere, *J. Geophys. Res.*, *86*, 11,148, doi:10.1029/JA086iA13p11148.

Hewett, D. W. (1985), Elimination of electromagnetic radiation in plasma simulation: The Darwin or magnetoinductive approximation, *Space Sci. Rev.*, *42*, 29, doi:10.1007/BF00218221.

Horne, R. B. (2007), Acceleration of killer electrons, *Nat. Phys.*, *3*, 590, doi:10.1038/nphys703.

Horne, R. B., and R. M. Thorne (1998), Potential waves for relativistic electron scattering and stochastic acceleration during magnetic storms, *Geophys. Res. Lett.*, *25*, 3011, doi:10.1029/98GL01002.

Horne, R. B., S. A. Glauert, and R. M. Thorne (2003), Resonant diffusion of radiation belt electrons by whistler-mode chorus, *Geophys. Res. Lett.*, *30*(9), 1493, doi:10.1029/2003GL016963.

Horne, R. B., R. M. Thorne, S. A. Glauert, J. M. Albert, N. P. Meredith, and R. R. Anderson (2005), Timescale for radiation belt electron acceleration by whistler mode chorus, *J. Geophys. Res.*, *110*, A03225, doi:10.1029/2004JA010811.

Kadomtsev, B. B., and O. P. Pogutse (1967), Electric conductivity of a plasma in a strong magnetic field, *Sov. Phys. JETP, Engl. Transl.*, *26*, 1146.

Kasahara, Y., Y. Miyoshi, Y. Omura, O. P. Verkhoglyadova, I. Nagano, I. Kimura, and B. T. Tsurutani (2009), Simultaneous satellite observations of VLF chorus, hot and relativistic electrons in a magnetic storm of "recovery" phase, *Geophys. Res. Lett.*, *36*, L01106, doi:10.1029/2008GL036454.

Kennel, C. F., and H. E. Petschek (1966), Limit on stably trapped particle fluxes, *J. Geophys. Res.*, *71*, 1.

LeDocq, M. J., D. A. Gurnett, and G. B. Hospodarsky (1998), Chorus source locations from VLF Poynting flux measurements with the Polar spacecraft, *Geophys. Res. Lett.*, *25*, 4063, doi:10.1029/1998GL900071.

Le Quéau, D., and A. Roux (1987), Quasi-monochromatic wave-particle interactions in magnetospheric plasmas, *Sol. Phys.*, *111*, 59, doi:10.1007/BF00145441.

Li, W., et al. (2010), THEMIS analysis of observed equatorial electron distributions responsible for chorus excitation, *J. Geophys. Res.*, *115*, A00F11, doi:10.1029/2009JA014845.

Lorentzen, K. R., J. B. Blake, U. S. Inan, and J. Bortnik (2001), Observations of relativistic electron microbursts in association with VLF chorus, *J. Geophys. Res.*, *106*, 6017, doi:10.1029/2000JA003018.

Meredith, N. P., R. B. Horne, and R. R. Anderson (2001), Substorm dependence of chorus amplitudes: Implications for the acceleration of electrons to relativistic energies, *J. Geophys. Res.*, *106*(A7), 13,165, doi:10.1029/2000JA900156.

Meredith, N. P., R. B. Horne, R. M. Horne, and R. R. Anderson (2009), Survey of upper band chorus and ECH waves: Implications for diffuse aurora, *J. Geophys. Res.*, *114*, A07218, doi:10.1029/2009JA014230.

Nunn, D., Y. Omura, H. Matsumoto, I. Nagano, and S. Yagitani (1997), The numerical simulations of VLF chorus and discrete emissions observed on the Geotail satellite using a Vlasov code, *J. Geophys. Res.*, *102*, 27,083, doi:10.1029/97JA02518.

Nunn, D., O. Santolik, M. Rycroft, and V. Trakhtengerts (2009), On the numerical modeling of VLF chorus dynamical spectra, *Ann. Geophys.*, *27*, 2341, doi:10.5194/angeo-27-2341-2009.

Ober, D. M., J. L. Horwitz, and D. L. Gallagher (1998), Convection of plasmaspheric plasma into the outer magnetosphere and boundary layer region: Initial results, in *Geospace Mass and Energy Flow: Results from the International Solar-Terrestrial Physics Program*, *Geophys. Monogr. Ser.*, vol. 104, edited by J. L. Horwitz, D. L. Gallagh, and W. K. Peterson, pp. 45–50, AGU, Washington, D. C.

Omelchenko, Y. A., V. D. Shapiro, V. I. Shevchenko, M. Ashour-Abdalla, and D. Schriver (1994), Modified lower hybrid fan instability excited by precipitating auroral electrons, *J. Geophys. Res.*, *99*, 5965, doi:10.1029/93JA01323.

Omura, Y., N. Furuya, and D. Summers (2007), Relativistic turning acceleration of resonant electrons by coherent whistler mode waves in a dipole magnetic field, *J. Geophys. Res.*, *112*, A06236, doi:10.1029/2006JA012243.

Omura, Y., Y. Katoh, and D. Summers (2008), Theory and simulation of the generation of whistler-mode chorus, *J. Geophys. Res.*, *113*, A04223, doi:10.1029/2007JA012622.

Omura, Y., M. Hikishima, Y. Katoh, D. Summers, and S. Yagitani (2009), Nonlinear mechanisms of lower-band and upper-band VLF chorus emissions in the magnetosphere, *J. Geophys. Res.*, *114*, A07217, doi:10.1029/2009JA014206.

Parrot, M., O. Santolik, N. Cornilleau-Wehrlin, M. Maksimovic, and C. Harvey (2003a), Source location of chorus emissions observed by Cluster, *Ann. Geophys.*, *21*, 473, doi:10.5194/angeo-21-473-2003.

Parrot, M., O. Santolik, N. Cornilleau-Wehrlin, M. Maksimovic, and C. Harvey (2003b), Magnetospherically reflected chorus waves revealed by ray tracing with CLUSTER data, *Ann. Geophys.*, *21*, 1111, doi:10.5194/angeo-21-1111-2003.

Parrot, M., O. Santolik, D. A. Gurnett, J. S. Pickett, and N. Cornilleau-Wehrlin (2004), Characteristics of magnetospherically reflected chorus waves observed by CLUSTER, *Ann. Geophys.*, *22*, 2597, doi:10.5194/angeo-22-2597-2004.

Rönnmark, K. (1982), WHAMP: Waves in a homogenous, anisotropic, multicomponent plasma, *Rep. 179*, Kiruna Geophys. Inst., Kiruna, Sweden.

Rönnmark, K. (1985), Kinetic theory of plasma waves, *Space Sci. Rev.*, *42*, 411, doi:10.1007/BF00214996.

Santolík, O. (2008), New results of investigations of whistler-mode chorus emissions, *Nonlin. Proc. Geophys.*, *15*, 621, doi:10.5194/npg-15-621-2008.

Santolík, O., D. A. Gurnett, and J. S. Pickett (2003a), Spatio-temporal structure of storm-time chorus, *J. Geophys. Res.*, *108*(A7), 1278, doi:10.1029/2002JA009791.

Santolík, O., M. Parrot, and F. Lefebvre (2003b), Singular value decomposition methods for wave propagation analysis, *Radio Sci.*, *38*(1), 1010, doi:10.1029/2000RS002523.

Santolík, O., D. A. Gurnett, J. S. Pickett, M. Parrot, and N. Cornilleau-Wehrlin (2004), A microscopic and nanoscopic view of storm-time chorus on 31 March 2001, *Geophys. Res. Lett.*, *31*, L02801, doi:10.1029/2003GL018757.

Santolík, O., D. A. Gurnett, J. S. Pickett, M. Parrot, and N. Cornilleau-Wehrlin (2005), Central position of the source region of storm-time chorus, *Planet. Space Sci.*, *53*, 299, doi:10.1016/j.pss.2004.09.056.

Santolík, O., D. A. Gurnett, J. S. Pickett, J. Chum, and N. Cornilleau-Wehrlin (2009), Oblique propagation of whistler-mode waves in the chorus source region, *J. Geophys. Res.*, *114*, A00F03, doi:10.1029/2009JA014586.

Santolík, O., D. A. Gurnett, J. S. Pickett, S. Grimald, P. M. E. Decreau, M. Parrot, N. Cornilleau-Wehrlin, F. El-Lemdani Mazouz, D. Schriver, and A. Fazakerley (2010), Wave-particle interactions in the equatorial source region of whistler-mode emissions, *J. Geophys. Res.*, doi:10.1029/2009JA015218, in press.

Sazhin, S. S., and M. Hayakawa (1992), Magnetospheric chorus emissions: A review, *Planet. Space Sci.*, *40*, 681, doi:10.1016/0032-0633(92)90009-D.

Shapiro, V. D., and V. I. Schevchenko (1968), Quasi-linear theory of relaxation of an electron beam in a magnetoactive plasma, *Sov. Phys. JETP, Engl. Transl.*, *27*, 635.

Shklyar, D., and H. Matsumoto (2009), Oblique whistler-mode waves in the inhomogeneous magnetospheric plasma: Resonant interactions with energetic charged particles, *Surv. Geophys.*, *30*, 55, doi:10.1007/s10712-009-9061-7.

Solomon, J., N. Cornilleau-Wehrlin, A. Korth, and G. Kremser (1988), An experimental study of ELF/VLF hiss generation in the Earth's magnetosphere, *J. Geophys. Res.*, *93*, 1839, doi:10.1029/JA093iA03p01839.

Summers, D., R. M. Thorne, and F. Xiao (1998), Relativistic theory of wave-particle resonant diffusion with application to electron acceleration in the magnetosphere, *J. Geophys. Res.*, *103*, 20,487, doi:10.1029/98JA01740.

Summers, D., B. Ni, and N. P. Meredith (2007), Timescales for radiation belt electron acceleration and loss due to resonant wave-particle interactions: 2. Evaluation for VLF chorus, ELF hiss and electromagnetic ion cyclotron waves, *J. Geophys. Res.*, *112*, A04207, doi:10.1029/2006JA011993.

Tsurutani, B. T., and E. J. Smith (1974), Postmidnight chorus: A substorm phenomenon, *J. Geophys. Res.*, *79*, 118, doi:10.1029/JA079i001p00118.

Tsurutani, B. T., and E. J. Smith (1977), Two types of magnetospheric ELF chorus and their substorm dependences, *J. Geophys. Res.*, *82*, 5112, doi:10.1029/JA082i032p05112.

Tsurutani, B. T., E. J. Smith, H. I. West Jr., and R. M. Buck (1979), Chorus, energetic electrons and magnetospheric substorms, in *Wave Instabilities in Space Plasmas*, edited by P. J. Palmadesso and K. Papadopoulos, pp. 55–63, Reidel Publ., Dordrecht, Netherlands.

Tsurutani, B. T., O. P. Verkhoglyadova, G. S. Lakhina, and S. Yagatani (2009), Properties of dayside outer zone chorus during HILDCAA events: Loss of energetic electrons, *J. Geophys. Res.*, *114*, A03207, doi:10.1029/2008JA013353.

Weiland, J., and H. Wilhelmsson (1976), *Coherent Nonlinear Interaction of Waves in Plasmas*, Pergamon, Oxford, U. K.

M. Ashour-Abdalla, F. V. Coroniti, and V. Decyk, Department of Physics and Astronomy, University of California, Los Angeles, CA 90095-1567, USA.

A. N. Fazakerley, Mullard Space Science Laboratory, University College London, Holmbury St. Mary RH5 6NT, UK.

M. L. Goldstein, Laboratory for Geospace Science, NASA Goddard Space Flight Center, Greenbelt, MD 20771, USA.

J. N. LeBoeuf, JNL Scientific, Casa Grande, AZ 85194-9695, USA.

J. S. Pickett, Department of Physics and Astronomy, University of Iowa, Office 715 Van Allen Hall, Iowa City, IA 52242, USA.

O. Santolík, Department of Space Physics, Institute of Atmospheric Physics, Boční II 1401, 141 31 Prah 4, Czech Republic.

D. Schriver, Institute of Geophysics and Planetary Physics, University of California, Los Angeles, CA 90095-1567, USA. (dave@igpp.ucla.edu)

P. Travnicek, Astronomical Institute, ASCR, Prague 14131, Czech Republic.

D. Winningham, Southwest Research Institute, PO Drawer 28510, San Antonio, TX 78228-0510, USA.